Acta Crystallographica Section B
**Structural Science**
ISSN 0108-7681

# Synthesis, characterization and phase transitions in the inorganic–organic layered perovskite-type hybrids $[(C_nH_{2n+1}NH_3)_2PbI_4]$, $n$ = 4, 5 and 6

**David G. Billing* and Andreas Lemmerer**

Molecular Sciences Institute, School of Chemistry, University of the Witwatersrand, Johannesburg, South Africa

Correspondence e-mail: dave.billing@wits.ac.za

Received 23 February 2007
Accepted 28 June 2007

Three inorganic–organic layered perovskite-type hybrids of the general formula $[(C_nH_{2n+1}NH_3)_2PbI_4]$, $n$ = 4, 5 and 6, display a number of reversible first-order phase transitions in the temperature range from 256 to 393 K. $[(C_4H_9NH_3)_2PbI_4]$ has a single phase transition, $[(C_5H_{11}NH_3)_2PbI_4]$ has two phase transitions and $[(C_6H_{13}NH_3)_2PbI_4]$ has three phase transitions. In all three cases, the lowest-temperature phase transition is thermochromic and the crystals change colour from yellow in their lowest-temperature phase to orange in their higher-temperature phase for $[(C_4H_9NH_3)_2PbI_4]$ and $[(C_6H_{13}NH_3)_2PbI_4]$, and from orange to red for $[(C_5H_{11}NH_3)_2PbI_4]$. The structural details associated with this phase transition have been investigated *via* single-crystal X-ray diffraction, SC-XRD, for all three compounds.

## 1. Introduction

Structural phase changes and polymorphism are two of the more significant and enigmatic problems in modern structural chemistry. When coupled with our lack of understanding and control of these phenomena, this results in major obstacles to the successful design of compounds with specific chemical and physical properties (Fernandes *et al.*, 2004; Dunitz, 1995). This is seen especially in inorganic–organic layered hybrid structures, which are able to combine desirable features from both types of constituents (Mitzi, 2001). Inorganic compounds have different band gaps and hence their electrical properties can vary from insulators to semiconductors and right the way through to superconductors. Furthermore, they supply the hybrid structure with thermal stability and hardness as well as magnetic and dielectric properties. The layered hybrid materials have been extensively studied for their excitonic and magneto-optical properties as they form natural quantum-well structures, especially $[(C_6H_{13}NH_3)_2PbI_4]$ (Tanaka *et al.*, 2002; Kataoka *et al.*, 1993*a*,*b*; Kondo, Iwamoto *et al.*, 1998; Shibuya *et al.*, 2002; Kondo, Azuma *et al.*, 1998; Tanaka *et al.*, 2005), $[(C_4H_9NH_3)_2PbBr_4]$ (Kato *et al.*, 2003) and under high pressure $[(C_8H_{17}NH_3)_2PbI_4]$ (Matsuishi *et al.*, 2004).

The two-dimensional hybrids, $[(R\text{-}NH_3)_2MX_4]$, where $R$ is a long-chain hydrocarbon, $M$ is a divalent metal and $X$ is a halogen, are based on the perovskite-like $K_2NiF_4$ or $RbAlF_4$ structure type. These inorganic compounds have staggered two-dimensional layers of corner-sharing $NiF_6$ octahedra or eclipsed two-dimensional layers of corner-sharing $AlF_6$ octahedra, which are separated by the $K^+$ or $Rb^+$ cations, respectively (Hatch & Stokes, 1987; Hatch *et al.*, 1989). In the inorganic–organic hybrids studied here, the two-dimensional layers consist of $MX_6$ octahedra and the cations are replaced by $RNH_3^+$ to form a laminar structure (Needham *et al.*, 1984), also referred to as a layered perovskite-type motif. The

organic cation can form bilayers between their organic layers if it has only one ammonium or a monolayer for two ammonium groups. Successive inorganic layers can either be staggered as in the $K_2NiF_4$ structure or they can be eclipsed, whereupon they are then based on the $RbAlF_4$ structure type. The organic cation ionically interacts and forms weak charge-assisted hydrogen bonds with the anionic inorganic layers.

Furthermore, the aliphatic materials $[(C_nH_{2n+1}NH_3)_2MX_4]$, here abbreviated as $C_nMX$, often exhibit a range of temperature-dependant structural phase transitions in the range from 235 K onwards for $n$ = 4, 8, 9 and 10 (Ishihara *et al.*, 1990), and above room temperature for $n$ = 12, 16 and 18 (Barman *et al.*, 2003), associated with changes in the ordering and hydrogen bonding of the organic cations. The crystals change colour from yellow to orange at the first transition temperature. The structural phase transitions observed can be displacive phase transitions, associated with conformational changes within the ammonium chains or order–disorder transitions of the ammonium chains along their longitudinal axis. The latter ultimately leads to a 'quasi-melting' of the hydrocarbon part (Chanh *et al.*, 1989) in the highest-temperature phases. The interlayer spacing increases with temperature as the rotational disordering increases (Barman *et al.*, 2003). The order–disorder transition is the only one observed when $n \leq 2$ and both transitions have been reported with chain lengths $n \geq 3$. The chain-melting transition is the major transition, usually the last one observed and with the highest enthalpy. Further, the conformation of the inorganic layers can change between eclipsed and staggered at the phase transitions and the degree of distortion of the octahedral geometry decreases with increasing temperature. The most obvious effect is often a change in the crystal system of the structure, from the monoclinic to the orthorhombic phase and finally the tetragonal at the highest temperature (Mitzi, 1999). One of the most intensely studied series of compounds is $[(C_3H_7NH_3)_2MCl_4]$ ($M$ = Cu, Cd and Mn). In these short-chain compounds, the structural transitions can be associated with the motion of the rigid propylammonium cation (Doudin & Chapuis, 1988, 1990; Depmeier *et al.*, 1977; Chapuis, 1978).

The objective of the present study was to determine the single-crystal structures of all the phases of the short-chain layered perovskite-type materials $[(C_nH_{2n+1}NH_3)_2PbI_4]$ ($n$ = 4, 5 and 6), as identified by differential scanning calorimetry and hot-stage microscopy (Fig. 1).

$$[(C_4H_9NH_3)_2PbI_4]:\ \mathbf{II}\ (1a^*) \underset{256.2\ K}{\overset{274.0\ K}{\rightleftarrows}} \mathbf{I}\ (1b^*)$$

$$[(C_5H_{11}NH_3)_2PbI_4]:\ \mathbf{III}\ (2b^*) \underset{315.4\ K}{\overset{318.6\ K}{\rightleftarrows}} \mathbf{II}\ (2c^*) \underset{390.0\ K}{\overset{391.2\ K}{\rightleftarrows}} \mathbf{I}$$

$$[(C_6H_{13}NH_3)_2PbI_4]:\ \mathbf{IV}\ (3a^{\S}) \underset{258\ K}{\overset{268\ K}{\rightleftarrows}} \mathbf{III}\ (3b^{*\S}) \underset{349.3\ K}{\overset{354.9\ K}{\rightleftarrows}} \mathbf{II}\ (3c^*) \underset{367.2\ K}{\overset{371.3\ K}{\rightleftarrows}} \mathbf{I}\ (3d^*)$$

**Figure 1**
Phase transitions as identified by DSC. Phase transitions labelled with a superscript * were single-to-single crystal and with superscript § were carried out on two different crystals.

## 2. Experimental

### 2.1. Crystal growth

**2.1.1. Preparation of $[(C_4H_9NH_3)_2PbI_4]$ (1).** $PbI_2$ (0.217 g, 0.471 mmol) was dissolved in 3 ml of 47% HI in a sample vial. Thereafter, 0.074 g of $C_4H_9NH_2$ (1.01 mmol) was added and the precipitate dissolved by refluxing for 2 h at 363 K. The solution was slowly cooled at 2 K $h^{-1}$ to room temperature. An orange single crystal suitable for X-ray diffraction analysis was selected and studied. Elemental analysis (%): calc. for $C_8H_{24}I_4N_2Pb_1$: C 11.13, H 2.80, N 3.25. Found: C 11.14, H 2.91, N 3.22.

**2.1.2. Preparation of $[(C_5H_{11}NH_3)_2PbI_4]$ (2).** $PbI_2$ (0.138 g, 0.065 mmol) was dissolved in 7 ml of 47% HI in a sample vial. Thereafter, 0.015 g of $C_5H_{11}NH_2$ (0.080 mmol) was added and the precipitate dissolved by refluxing for 2 h at 363 K. The solution was slowly cooled at 2 K $h^{-1}$ to room temperature. An orange single crystal suitable for X-ray diffraction analysis was selected and studied. Elemental analysis (%): calc. for $C_{10}H_{28}I_4N_2Pb_1$: C 13.48, H 3.17, N 3.14. Found: C 13.61, H 3.14, N 3.13.

**2.1.3. Preparation of $[(C_6H_{13}NH_3)_2PbI_4]$ (3).** $PbI_2$ (0.138 g, 0.065 mmol) was dissolved in 7 ml 47% HI in a sample vial. Thereafter, 0.015 g of $C_6H_{13}NH_2$ (0.080 mmol) was added and the precipitate dissolved by refluxing for 2 h at 363 K. The solution was slowly cooled at 2 K $h^{-1}$ to room temperature. An orange single crystal suitable for X-ray diffraction analysis was selected and studied. Elemental analysis (%): calc. for $C_{12}H_{32}I_4N_2Pb_1$: C 15.68, H 3.51, N 3.05. Found: C 15.98, H 3.35, N 3.11.

### 2.2. DSC measurements

Differential scanning calorimetry (DSC) data were collected on a Mettler Toledo 822$^e$ calorimeter at a scan rate of 5 K $min^{-1}$ in sealed aluminium pans under air.

### 2.3. X-ray crystallography

All diffraction data were collected on a Bruker Apex II CCD diffractometer (Bruker, 2005) with graphite-monochromated Mo $K\alpha$ radiation ($\lambda$ = 0.71073 Å). Collections carried out at non-ambient temperatures were performed using an Oxford Cryostream 700. Data reduction and cell refinement were carried out using *SAINT-PLUS* (Bruker, 2004) and space groups were determined from systematic absences by *XPREP* (Bruker, 2004) and further justified by the refinement results. Face-indexed absorption corrections were performed on all crystals using *XPREP* (Bruker, 2004). In all cases, the structures were solved in the *WinGx* suite of programs (Farrugia, 1999) by direct methods using *SHELXS*97 (Sheldrick, 1997*a*) and refined using full-matrix least-squares calculations based on $F^2$ using *SHELXL*97 (Sheldrick, 1997*b*). All non-H atoms were refined with anisotropic displacement parameters. Bond lengths and angles in the chains were restrained to ideal geometries. After that, all H atoms were placed at idealized positions with isotropic displacement parameters, relative to those of the heavy atoms

**Table 1**
Crystal data.

| | (1*a*), (II) | (1*b*), (I) | (2*a*), (III) | (2*b*), (III) | (2*c*), (II) |
|---|---|---|---|---|---|
| Crystal data | | | | | |
| Chemical formula | $2C_4H_{12}N{\cdot}I_4Pb$ | $2C_4H_{12}N{\cdot}I_4Pb$ | $2C_5H_{14}N{\cdot}I_4Pb$ | $2C_5H_{14}N{\cdot}I_4Pb$ | $2C_5H_{14}N{\cdot}I_4Pb$ |
| $M_r$ | 863.08 | 863.08 | 891.13 | 891.13 | 891.13 |
| Cell setting, space group | Orthorhombic, *Pbca* | Orthorhombic, *Pbca* | Monoclinic, $P2_1/a$ | Monoclinic, $P2_1/a$ | Orthorhombic, *Pbca* |
| Temperature (K) | 223 (2) | 293 (2) | 173 (2) | 293 (2) | 333 (2) |
| *a*, *b*, *c* (Å) | 8.428 (2), 8.986 (2), 26.233 (6) | 8.8764 (1), 8.6925 (1), 27.6014 (5) | 8.472 (2), 9.007 (2), 14.784 (3) | 8.6716 (7), 8.9297 (6), 14.8805 (13) | 9.0078 (10), 8.7310 (10), 29.956 (4) |
| $\beta$ (°) | 90 | 90 | 100.881 (4) | 100.212 (2) | 90 |
| $V$ (Å$^3$) | 1986.7 (17) | 2129.67 (5) | 1107.8 (4) | 1134.01 (15) | 2356.0 (5) |
| $Z$ | 4 | 4 | 2 | 2 | 4 |
| $D_x$ (Mg m$^{-3}$) | 2.886 | 2.692 | 2.671 | 2.61 | 2.512 |
| $\mu$ (mm$^{-1}$) | 14.69 | 13.71 | 13.18 | 12.87 | 12.39 |
| Crystal form, colour | Cube, yellow | Cube, orange | Plate, orange | Plate, orange | Plate, red |
| Crystal size (mm) | 0.14 × 0.13 × 0.08 | 0.15 × 0.14 × 0.08 | 0.58 × 0.32 × 0.11 | 0.5 × 0.46 × 0.14 | 0.5 × 0.45 × 0.14 |
| Data collection | | | | | |
| Diffractomter | Bruker APEXII CCD area detector | Bruker APEXII CCD area detector | Bruker APEXII CCD area detector | Bruker APEXII CCD area detector | Bruker APEXII CCD area detector |
| Data collection method | $\omega$ scans | $\omega$ scans | $\omega$ scans | $\omega$ scans | $\omega$ scans |
| Absorption correction | Integration | Integration | Integration | Integration | Integration |
| $T_{min}$ | 0.165 | 0.160 | 0.035 | 0.020 | 0.017 |
| $T_{max}$ | 0.339 | 0.359 | 0.241 | 0.179 | 0.176 |
| No. of measured, independent and observed reflections | 7581, 1745, 1500 | 15 579, 1981, 1541 | 7043, 2649, 2334 | 8718, 2734, 2259 | 11 216, 2194, 1566 |
| Criterion for observed reflections | $I > 2\sigma(I)$ | $I > 2\sigma(I)$ | $I > 2\sigma(I)$ | $I > 2\sigma(I)$ | $I > 2\sigma(I)$ |
| $R_{int}$ | 0.083 | 0.079 | 0.080 | 0.055 | 0.066 |
| $\theta_{max}$ (°) | 25.0 | 25.5 | 28 | 28 | 25.5 |
| Refinement | | | | | |
| Refinement on | $F^2$ | $F^2$ | $F^2$ | $F^2$ | $F^2$ |
| $R[F^2 > 2\sigma(F^2)]$, $wR(F^2)$, $S$ | 0.101, 0.27, 1.38 | 0.38, 0.076, 1.13 | 0.038, 0.105, 1.15 | 0.044, 0.121, 1.07 | 0.124, 0.284, 1.32 |
| No of reflections | 1745 | 1981 | 2649 | 2734 | 2194 |
| No. of parameters | 70 | 71 | 79 | 79 | 79 |
| H-atom treatment | Constrained to parent site | Constrained to parent site | Constrained to parent site | Constrained to parent site | Constrained to parent site |
| Weighting scheme | $w = 1/[\sigma^2(F_o^2) + 573.3984P]$, where $P = (F_o^2 + 2F_c^2)/3$ | $w = 1/[\sigma^2(F_o^2) + (0.0196P)^2 + 10.8314P]$, where $P = (F_o^2 + 2F_c^2)/3$ | $w = 1/[\sigma^2(F_o^2) + (0.0375P)^2 + 8.7673P]$, where $P = (F_o^2 + 2F_c^2)/3$ | $w = 1/[\sigma^2(F_o^2) + (0.0576P)^2 + 5.635P]$, where $P = (F_o^2 + 2F_c^2)/3$ | $w = 1/[\sigma^2(F_o^2) + 291.1164P]$, where $P = (F_o^2 + 2F_c^2)/3$ |
| $(\Delta/\sigma)_{max}$ | < 0.0001 | 0.001 | 0.001 | 0.001 | 0.001 |
| $\Delta\rho_{max}$, $\Delta\rho_{min}$ (e Å$^{-3}$) | 3.92, −5.67 | 0.82, −1.15 | 1.50, −2.67 | 1.90, −2.07 | 2.17, −2.67 |
| Extinction method | None | *SHELXL* | None | None | None |
| Extinction coefficient | – | 0.00341 (14) | – | – | – |

| | (3*a*), (IV) | (3*b*), (III) | (3*c*), (II) | (3*d*), (I) |
|---|---|---|---|---|
| Crystal data | | | | |
| Chemical formula | $2C_6H_{16}N{\cdot}I_4Pb$ | $2C_6H_{16}N{\cdot}I_4Pb$ | $2C_6H_{16}N{\cdot}I_4Pb$ | $2C_6H_{16}N{\cdot}I_4Pb$ |
| $M_r$ | 919.19 | 919.19 | 919.19 | 919.19 |
| Cell setting, space group | Monoclinic, $P2_1/a$ | Orthorhombic, *Pbca* | Orthorhombic | Tetragonal |
| Temperature (K) | 173 (2) | 293 (2) | 358(2) | 378(2) |
| *a*, *b*, *c* (Å) | 8.643 (4), 8.845 (4), 16.052 (7) | 8.9413 (2), 8.6874 (2), 32.7027 (10) | 8.6606 (8), 8.8215 (8), 35.2423 (36) | 8.7632 (3), 8.7632 (3), 34.0586 (19) |
| $\beta$ (°) | 91.985 (8) | 90 | 90 | 90 |
| $V$ (Å$^3$) | 1226.4 (9) | 2540.24 (11) | 2692.50 (77) | 2615.47 (32) |
| $Z$ | 2 | 4 | 4 | 4 |
| $D_x$ (Mg m$^{-3}$) | 2.489 | 2.403 | | |
| Radiation type | Mo $K\alpha$ | Mo $K\alpha$ | Mo $K\alpha$ | Mo $K\alpha$ |
| $\mu$ (mm$^{-1}$) | 11.91 | 11.50 | – | – |
| Crystal form, colour | Plate, yellow | Plate, orange | Plate, red | Plate, red |
| Crystal size (mm) | 0.32 × 0.16 × 0.02 | 0.46 × 0.28 × 0.05 | 0.46 × 0.28 × 0.05 | 0.46 × 0.28 × 0.05 |
| Data collection | | | | |
| Diffractometer | Bruker APEXII CCD area detector | Bruker APEXII CCD area detector | – | – |
| Data collection method | $\omega$ scans | $\omega$ scans | – | – |
| Absorption correction | Integration | Integration | – | – |

**Table 1 (continued)**

| | (3*a*), (IV) | (3*b*), (III) | (3*c*), (II) | (3*d*), (I) |
|---|---|---|---|---|
| $T_{min}$ | 0.147 | 0.058 | – | – |
| $T_{max}$ | 0.784 | 0.536 | – | – |
| No. of measured, independent and observed reflections | 11 777, 2984, 2563 | 12 552, 3056, 2421 | – | – |
| Criterion for observed reflections | $I > 2\sigma(I)$ | $I > 2\sigma(I)$ | – | – |
| $R_{int}$ | 0.092 | 0.045 | – | – |
| $\theta_{max}$ (°) | 28 | 28 | – | – |
| Refinement | | | | |
| Refinement on | $F^2$ | $F^2$ | – | – |
| $R[F^2 > 2\sigma(F^2)]$, $wR(F^2)$, $S$ | 0.059, 0.143, 1.21 | 0.081, 0.168, 1.34 | – | – |
| No. of reflections | 2984 | 3056 | – | – |
| No. of parameters | 89 | 89 | – | – |
| H-atom treatment | Constrained to parent site | Constrained to parent site | – | – |
| Weighting scheme | $w = 1/[\sigma^2(F_o^2) + (0.0221P)^2 + 49.3157P]$, where $P = (F_o^2 + 2F_c^2)/3$ | $w = 1/[\sigma^2(F_o^2) + 101.7161P]$, where $P = (F_o^2 + 2F_c^2)/3$ | – | – |
| $(\Delta/\sigma)_{max}$ | 0.002 | 0.001 | – | – |
| $\Delta\rho_{max}$, $\Delta\rho_{min}$ (e Å$^{-3}$) | 4.91, −1.94 | 1.65, −1.69 | – | – |
| Extinction method | None | *SHELXL* | – | – |
| Extinction coefficient | - | 0.00037(4) | – | – |

Computer programs used: *APEX*2 (Bruker, 2005), *SAINT-Plus* and *XPREP* (Bruker, 2004), *SHELXS*97 (Sheldrick, 1997*a*), *SHELXL*97 (Sheldrick, 1997*b*), *ORTEP*3 for Windows (Farrugia, 1997), *DIAMOND* (Brandenburg, 1999), *WinGX* publication routines (Farrugia, 1999), *PLATON* (Spek, 2003).

to which they were attached [$U_{iso}$(H) = 1.2$U_{eq}$(C) or 1.5$U_{eq}$(N) or 1.5$U_{eq}$(C)]. The H atoms on the N atom are placed in idealized positions, staggered with respect to the shortest other bond to the atom to which the $NH_3^+$ is attached. This optimizes the hydrogen-bonding contacts.

In all the reported crystal structures, the fractional coordinates of the Pb atom in the asymmetric unit were chosen to be at the special position (1,1,1). This aids in the comparison of related structures. The crystal structures (2*a*), (2*b*) and (3*a*), that crystallized in a monoclinic system, were refined in the non-standard setting $P2_1/a$ of space group $P2_1/c$ so that a direct comparison among cell dimensions is possible when compared with the crystal structures of (2*c*) and (3*b*).

The carbon distances in (1*b*), (2*b*), (2*c*) and (3*b*), whose intensity data were collected at room and higher temperatures, were unusual as a result of the thermal motion of the carbon chains. The C—C distances were then restrained in *SHELX* to reasonable molecular geometries and the anisotropic displacement parameters restrained to be equal in the direction of the bonds. The below-room-temperature structure (1*a*) had restraints on the thermal ellipsoids and (2*a*) and (3*a*) required no restraints at all. The crystal structure of (3*a*) required a twinned refinement.

Experimental details of the X-ray analyses are provided in Table 1[1] and the atomic numbering schemes in Fig. 2. Diagrams and publication material were generated using *ORTEP* (Farrugia, 1997), *PLATON* (Spek, 2003), *DIAMOND* (Brandenburg, 1999) and *WinGx* (Farrugia, 1999).

[1] Supplementary data for this paper are available from the IUCr electronic archives (Reference: BS5044). Services for accessing these data are described at the back of the journal.

## 3. Results and discussion

The series of compounds investigated in this paper show changes in the position of the alkylammonium chains relative to the inorganic layer as a consequence of phase changes. The compounds $[(C_5H_{11}NH_3)_2PbI_4]$, hereafter $C_5PbI$, and $[(C_6H_{13}NH_3)_2PbI_4]$, $C_6PbI$, additionally show relative movements of the inorganic layers, containing the corner-shared lead iodide octahedra. These shifts of the inorganic layers result in changes in the crystal system of the compounds. $C_6PbI$ is monoclinic in phase (IV) and orthorhombic in phase (III). Similarly, $C_5PbI$ changes from monoclinic (III) to orthorhombic (II). $[(C_4H_9NH_3)_2PbI_4]$, $C_4PbI$, is the exception and is orthorhombic in both phases (II) and (I) with no observable shift in the layers. Only the low-temperature phase transition of each compound was investigated structurally. The high-temperature phase transition of $C_5PbI$ was beyond the capabilities of the heating device. For $C_6PbI$, the phase transitions at the higher temperatures unfortunately lead to fracturing of the crystals studied. As a consequence it was not feasible to collect data of a quality suitable for structure refinement, hence only unit-cell dimensions were determined.

Doudin & Chapuis (1990) introduced a geometric quantity for their discussion of the phase changes of $[(C_3H_7NH_3)_2CuCl_4]$; the tilt $\angle_\varphi$ of the organic chains, 'which defines the rotation angle of the N—C3 axis'. In this paper we extend the definition of the tilt $\angle_\varphi$ to be the angle between a plane through the inorganic layers and a vector connecting the first and last atom of each chain, for example, the N1 atom and the C4 atom in the case of $C_4PbI$. Two further quantities are required to track the motion of the alkylammonium chains before and after the phase transition: an angle $\angle_\alpha$, which is defined as the dihedral angle between a plane containing all

the atoms of the alkylammonium chains and the plane formed by the lead atoms of the inorganic layers; and an angle $\angle_\beta$, which is defined as the angle between a vector connecting the atoms N1 and C1 and a plane through the lead atoms of the inorganic layers (see Fig. 3).

The position of the ammonium group is affected by the phase changes and consequently affects the hydrogen-bonding configuration. The 'box' containing the ammonium groups is defined by the four equatorial, or bridging iodides, and the four axial, or terminal iodides that protrude above the layer. In projection, the ammonium group is contained within a parallelogram defined by the four bridging iodides (see Fig. 4). By projection onto this parallelogram the ammonium group is found in proximity to either an acute or an obtuse angle of the parallelogram.

It has been found that the three H atoms associated with the ammonium group either bond to two terminal iodides and one bridging iodide (terminal halogen configuration) or to two bridging iodides and one terminal iodide (bridging halogen configuration; Mitzi, 1999). All the compounds described here in all their phases adopt the terminal halogen configuration. However, there are two ways that the H atoms can adopt the terminal halogen configuration: the three iodides to which the H atoms bond can be at the vertices of either an equilateral triangle or a right-angle triangle (see Fig. 4). There is a correlation between the position of the ammonium group and the type of terminal halogen configuration: if the ammonium group is in the acute angled position, it has the right-angled configuration and if the ammonium group is in the obtuse angled position, it has the equilateral configuration. The phase changes we observe for $C_4PbI$ and $C_5PbI$ are associated with the interconversion between these two geometries.

The corner-sharing $PbI_6$ octahedra that make up the two-dimensional layers are affected by the phase changes. For the layered perovskite-type hybrids, two out of a three possible tilts are encountered (Hatch *et al.*, 1989). Firstly, a tilt perpendicular to the inorganic sheets ($\theta$ tilt), so that adjacent corner-shared octahedra are rotated relative to each other. The angle of the $\theta$ tilt is mirrored in the bridging angle Pb—I—Pb, which deviates from 180°. The second kind of tilt is parallel to the layers ($\Psi$ tilt), so that the layers are corrugated in one direction. The corrugation angle is measured by the angle between the normal to the inorganic layers and the vector connecting the Pb atom and the terminal I.

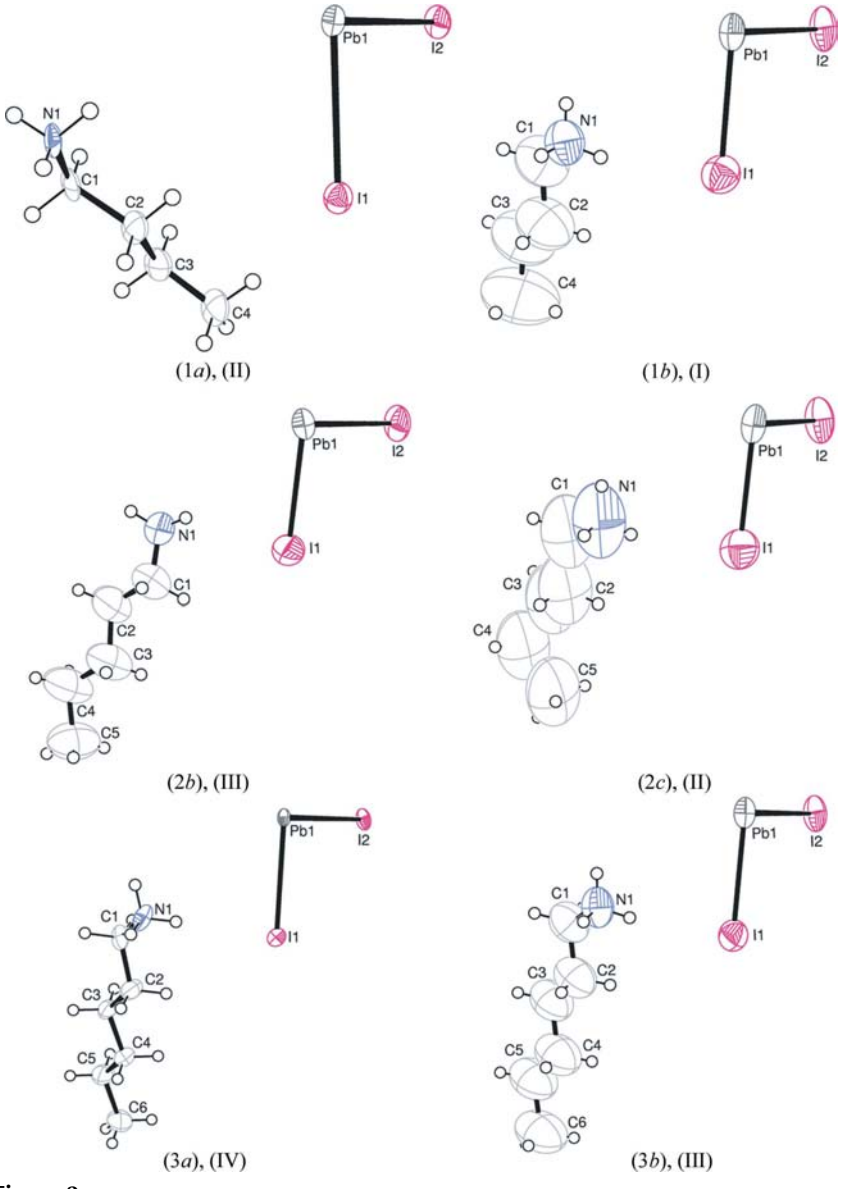


**Figure 2**
The asymmetric unit and atomic numbering scheme of the three compounds (1)–(3). The structures of the compounds in their lowest-temperature phase are shown in the left column, labelled (1*a*), (2*b*) and (3*a*), and their respective higher-temperature phases are shown on the right, labelled (1*b*), (2*c*) and (3*b*). The anisotropic displacement parameters are shown at the 50% probability level.

### 3.1. Thermal analysis studies

All the three compounds studied showed multiple reversible phase transitions (Fig. 5) when studied by DSC (see Table 2). The phase transitions are numbered consecutively $T_1$, $T_2$ *etc.* with increasing temperature. Hysteresis causes some variation in the actual transition temperatures and hence the superscript $^h$ is added when the crystals were heated or the superscript $^c$ when the crystals were cooled.

**3.1.1. $[(C_4H_9NH_3)_2PbI_4]$ (1).** Thermal analysis of $C_4PbI$ *via* DSC revealed one endotherm when heating, at $T_1^h$ = 273.8 K, and one exotherm when cooling, $T_1^c$ = 256 K. The exothermic peak is shifted by almost

**Table 2**
DSC scan details and values of the phase transitions after heating and cooling.

| Chain length | Heating | Cooling |
|---|---|---|
| $n = 4$ | | |
| $T_1$ (°C, K) | 0.8 (274.0) | −17.0 (256.2) |
| $\Delta H$ (kJ mol$^{-1}$) | 9.5 | 12.5 |
| $n = 5$ | | |
| $T_1$ (°C, K) | 45.4 (318.6) | 42.3 (315.4) |
| $\Delta H_1$ (kJ mol$^{-1}$) | 6.0 | 7.8 |
| $T_2$ (°C, K) | 118.1 (391.2) | 116.8 (390.0) |
| $\Delta H_2$ (kJ mol$^{-1}$) | 0.56 | 0.71 |
| $n = 6$ | | |
| $T_1$ (°C, K) | −4 to −8 (269–265) and 45 (313) | −16 to −22 (257–251) |
| $\Delta H_1$ (kJ mol$^{-1}$) | 0.435 | 0.539 |
| $T_2$ (°C, K) | 81.7 (354.9) | 76.1 (349.3) |
| $\Delta H_2$ (kJ mol$^{-1}$) | 13.5 | 12.7 |
| $T_3$ (°C, K) | 98.1 (371.3) | 94.0 (367.2) |
| $\Delta H_3$ (kJ mol$^{-1}$) | 1.1 | 1.2 |

18 K lower compared with the endothermic peak, which is evidence of severe thermal hysteresis. The phase transition is accompanied by a change in crystal colour (see Fig. 6). The crystals are orange at room temperature. The colour remains unchanged until the phase transition. Then, the colour change is sudden and the crystal is yellow with significant fractures visible on the surface. $C_4PbI$ shows no additional phase behaviour up to thermal decomposition. The DSC scans showed small peaks at 255 (*endo*), 358 (*exo*) and 418 K (*endo*). These peaks could either be due to sample movement in the aluminium pan or minor structural rearrangements of the $C_4PbI$ compound itself.

**3.1.2. $[(C_5H_{11}NH_3)_2PbI_4]$ (2).** Thermal analysis of $C_5PbI$ *via* DSC revealed two endotherms at $T_1^h$ = 318.4 K and $T_2^h$ = 391.1 K when heating the sample, and two exotherms when cooling. The exothermic peaks are shifted to lower temperatures relative to the endothermic peaks, which is evidence of thermal hysteresis. The values of the enthalpies of the endotherms on the cooling cycle are slightly lower.

Hot-stage microscope pictures were taken before and after the first phase transition. The colour of the crystal is orange at room temperature. The colour darkens with temperature until the first phase transition. Then, the colour change is sudden and the crystals turn reddish orange. When the rate of heating

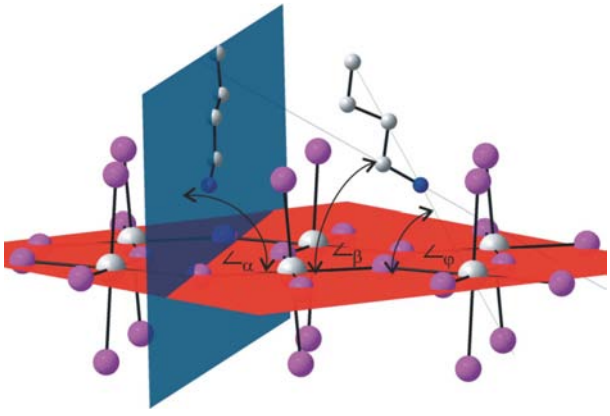


**Figure 3**
The geometric quantities used for characterizing the cation orientation relative to the inorganic layers. The least-squares plane through the lead atoms is shown in red and the least-squares plane through the C and N atoms of the alkylammonium cations is shown in blue.

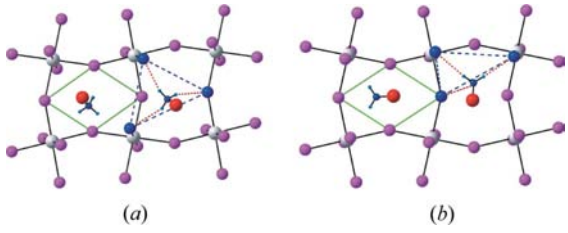


**Figure 4**
The picture on the left shows the position of the ammonium group near the obtuse angle of the parallelogram, shown in green, and the equilateral configuration, shown in blue. The picture on the right shows the alternative case.

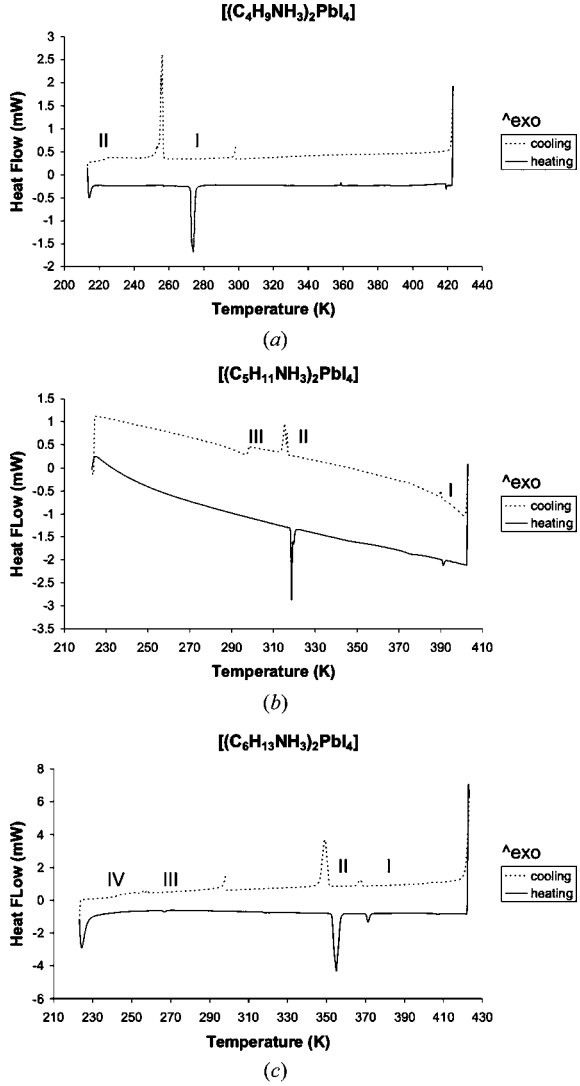


**Figure 5**
DSC scans of the reversible phase transitions for the compounds (*a*) (1), (*b*) (2) and (*c*) (3), including phase labelling.

is slow, a distinct, red colour wave runs through the crystal (see Fig. 7). The enthalpy for this transition is much greater than for the second transition. The colour of the crystal after the last phase change is a more intense red.

**3.1.3. $[(C_6H_{13}NH_3)_2PbI_4]$ (3)**. Ishihara *et al.* (1990) has investigated the optical spectra of $(C_6H_{13}NH_3)_2PbI_4$ ($C_6PbI$) and found no evidence suggesting the existence of any structural phase transitions between ambient and liquid-helium temperature. However, DSC scans carried out between 223 and 433 K show a series of small exothermic peaks starting at $T_1^c$ = 258 K and small endothermic peaks at $T_1^h$ = 269 to 265 K (see Fig. 8) and a further small peak at 318 K. These peaks result from the inorganic layers shifting relative to each other, resulting in a change in symmetry from monoclinic to orthorhombic, together with a doubling of the unit-cell parameter perpendicular to the layer shift. Additional DSC char-

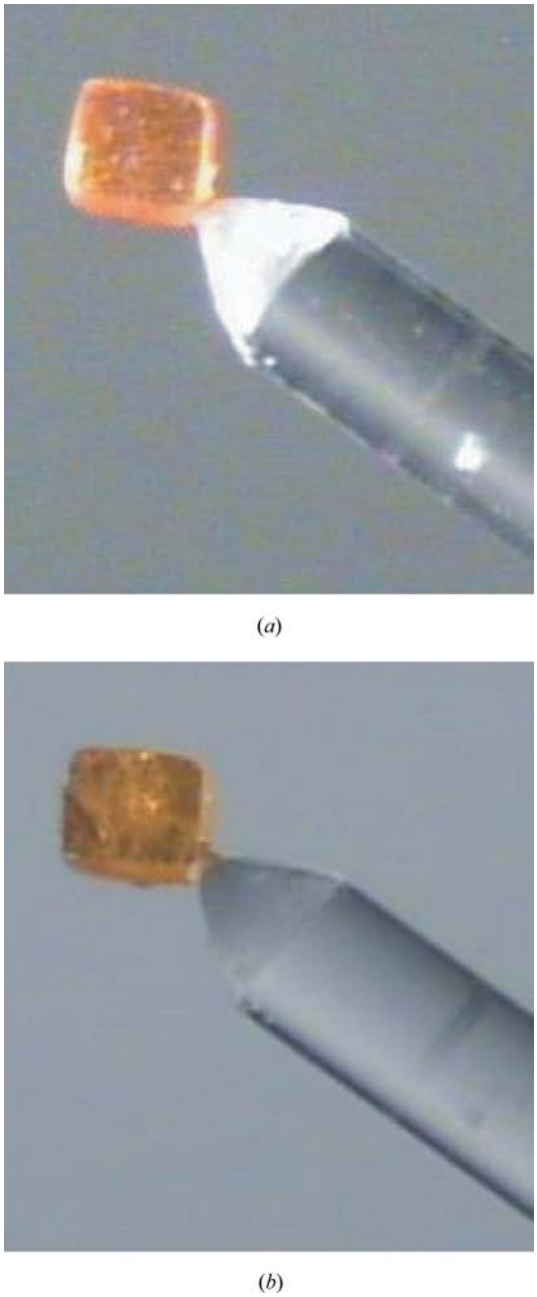

**Figure 6**
The crystal of $[(C_4H_9NH_3)_2PbI_4]$ used in the diffraction experiment. (*a*) Phase (I) (270 K) and (*b*) (II) (223 K).

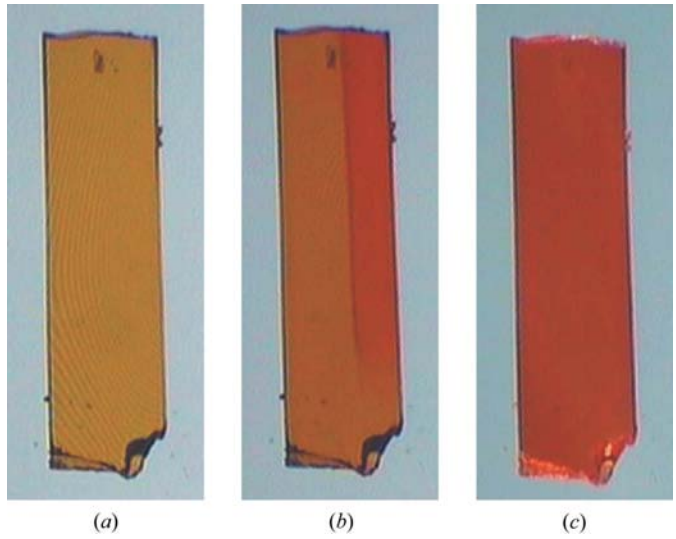

**Figure 7**
Hot-stage microscope pictures of a crystal of $[(C_5H_{11}NH_3)_2PbI_4]$ under polarized light. Photograph (*a*) shows the crystal at room temperature [phase (III)], (*b*) at the phase transition temperature of 318 K where the new phase is encroaching from the right, and (*c*) after the phase change is complete [phase (II)].

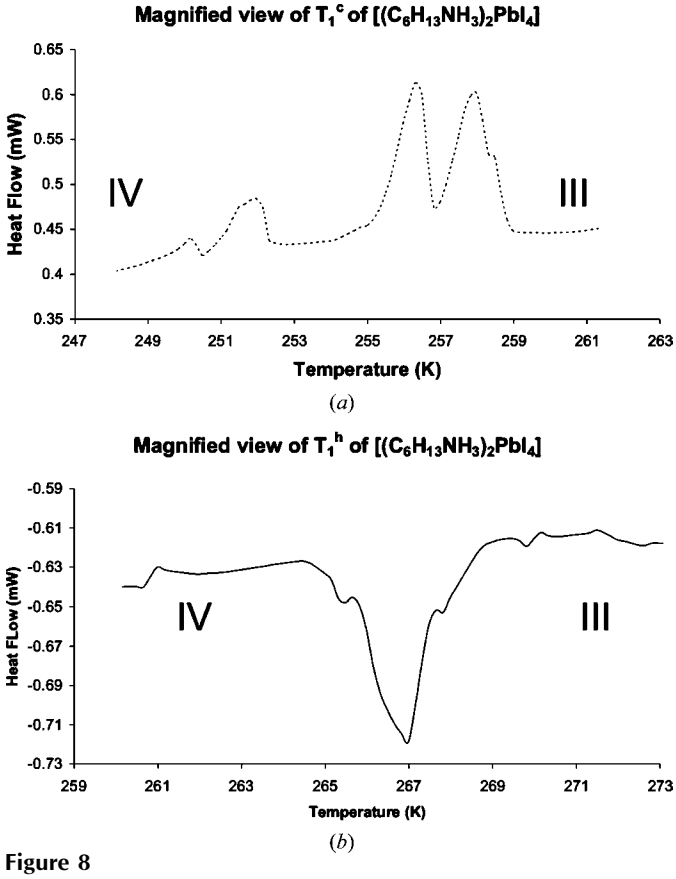


**Figure 8**
Magnified view of the first phase transition of $C_6PbI$ in (*a*) the cooling and (*b*) the heating cycle.

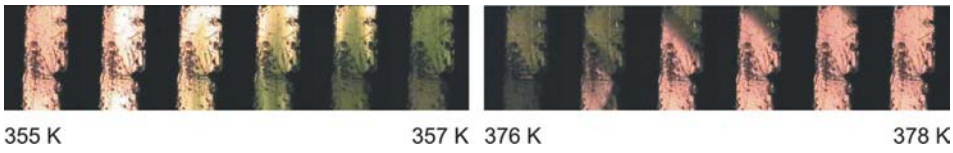


**Figure 9**
Optical microscopy shows the visual evidence for the phase transitions of $(C_6H_{13}NH_3)_2PbI_4$ at 355 K [(III) to (II)] and 376 K [(II) to (I)].

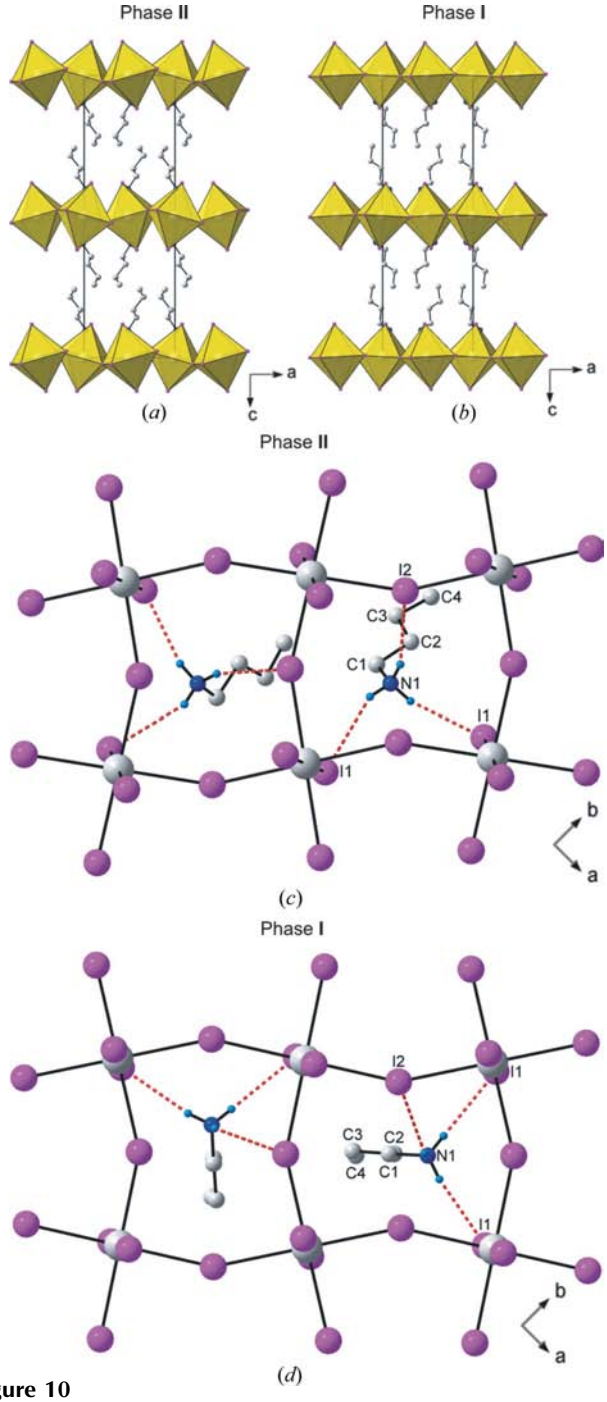


**Figure 10**
The two phases of $C_4PbI$ are shown. Packing diagrams of (II) at (*a*) 223 K and (*b*) (I) at 293 K. The hydrogen-bonding scheme and orientation of the butylammonium chains in phase (II) is shown in (*c*) and of phase (I) in (*d*). The equilateral and right-angled configuration is clearly seen in (*c*) and (*d*), respectively. H atoms on C atoms are omitted for clarity.

acterization revealed two further major endotherms at $T_2^h$ = 354.7 K and $T_3^h$ = 371.1 K when heating the sample, and two exotherms when cooling. On average, the exotherms are 5 and 4 K lower than the endotherms.

Hot-stage microscope pictures were taken before and after the second and third phase transitions. The crystals are orange at room temperature. The colour darkens with temperature until the second phase transition, where the colour suddenly changes to a reddish orange. When the rate of heating is slow, a wavefront propagating the newly formed phase is discernible (see Fig. 9). The enthalpy for this transition is much greater than that for the second transition. The colour of the crystal after the last phase change is again a more intense red, similar to $C_5PbI$. The colour change associated with the phase transition below room temperature is from orange to yellow.

### 3.2. Structural aspects of the thermochromic phase transitions of $C_4PbI$, $C_5PbI$ and $C_6PbI$

**3.2.1. Discussion of the phase transition of $C_4PbI$ (II) [(1*a*)] to (I) [(1*b*)].** The crystal structure of the lowest temperature phase, (II) of $C_4PbI$, designated (1*a*), was determined at 223 K, and the room-temperature structure of phase (I), at 293 K, is designated (1*b*). Figs. 10(*a*) and (*b*) clearly show a bidimensional arrangement in which two layers of interdigitated butylammonium cations are embedded between two consecutive inorganic $[PbI_6]$ sheets, forming an alternate inorganic–organic layered structure. The Pb atoms are offset from layer to layer in both phases (II) and (I), resulting in a staggered arrangement of adjacent layers, thus displaying the $K_2NiF_4$ structure type. In the direction perpendicular to the layers, the crystal cohesion is achieved by ionic interactions and by N—H···I hydrogen bonds, related to the $NH_3^+$ ammonium groups. There are only weak van der Waals forces between two adjacent cations [nearest-neighbour distances are 4.236 (0) Å for (II) and 4.073 (2) Å for (I)]. Within the inorganic layers, the crystal cohesion is achieved by strong interactions similar to those observed in $PbI_2$.

The inorganic layer of phase (II) [(1*a*)] is built up from characteristic corner-sharing $PbI_6$ octahedra. The asymmetric unit consists of a lead atom on a special position and two iodide atoms, I1 occupying the terminal position and I2 occupying the bridging position in the octahedra. As shown in the projection perpendicular to the layers in Fig. 10(*c*), along the *c* axis, the $PbI_6$ octahedra are rotated by 149.24 (10)° relative to each other, increasing to 155.07 (2)° in phase (I) (1*b*) (Fig. 10*d*). The bridging angle translates directly into the $\theta$ tilt, being 30.76 (10) and 24.93 (2)°, respectively, for (1*a*) and (1*b*). Furthermore, the perovskite layers in phase (II) are more corrugated in the *a* direction by an angle of $\Psi$ = 12.92 (4)° with respect to the *ab* plane compared with the room-temperature phase (I), $\Psi$ = 5.78 (2)°. The coordination geometry around the Pb atom shows axial compression of the

**Table 3**
Hydrogen-bonding details for compounds (1), (2) and (3) in their various phases.

| $D$—H$\cdots A$ | $D$—H (Å) | H$\cdots A$ (Å) | $D\cdots A$ (Å) | $\angle(D$—H$\cdots A)$ (°) |
|---|---|---|---|---|
| (1*a*), (II) | | | | |
| N1—H1*A*$\cdots$I1$^{i}$ | 0.90 | 3.01 | 3.65 (3) | 129 |
| N1—H1*B*$\cdots$I2$^{ii}$ | 0.90 | 2.79 | 3.65 (3) | 159 |
| N1—H1*C*$\cdots$I1$^{iii}$ | 0.90 | 2.71 | 3.58 (3) | 163 |
| (1*b*), (I) | | | | |
| N1—H1*A*$\cdots$I2$^{ii}$ | 0.89 | 2.97 | 3.619 (9) | 131 |
| N1—H1*B*$\cdots$I1 | 0.89 | 2.77 | 3.645 (9) | 166 |
| N1—H1*C*$\cdots$I1$^{iii}$ | 0.89 | 2.72 | 3.598 (9) | 171 |
| (2*a*), (III) | | | | |
| N1—H1*A*$\cdots$I1 | 0.91 | 2.84 | 3.594 (9) | 142 |
| N1—H1*B*$\cdots$I2$^{iv}$ | 0.91 | 2.81 | 3.658 (9) | 156 |
| N1—H1*C*$\cdots$I1$^{v}$ | 0.91 | 2.74 | 3.625 (9) | 166 |
| (2*b*), (III) | | | | |
| N1—H1*A*$\cdots$I1 | 0.89 | 2.85 | 3.59 (12) | 142 |
| N1—H1*B*$\cdots$I2$^{iv}$ | 0.89 | 2.89 | 3.721 (13) | 156 |
| N1—H1*C*$\cdots$I1$^{v}$ | 0.89 | 2.92 | 3.787 (15) | 166 |
| (2*c*), (II) | | | | |
| N1—H1*A*$\cdots$I2$^{ii}$ | 0.89 | 3.12 | 3.70 (5) | 125 |
| N1—H1*B*$\cdots$I1 | 0.89 | 2.80 | 3.66 (7) | 163 |
| N1—H1*C*$\cdots$I1$^{iii}$ | 0.89 | 2.65 | 3.53 (5) | 171 |
| (3*a*), (IV) | | | | |
| N1—H1*A*$\cdots$I2$^{iv}$ | 0.91 | 2.89 | 3.599 (13) | 136 |
| N1—H1*B*$\cdots$I1 | 0.91 | 2.75 | 3.650 (13) | 171 |
| N1—H1*C*$\cdots$I1$^{iv}$ | 0.91 | 2.69 | 3.553 (15) | 159 |
| (3*b*), (III) | | | | |
| N1—H1*A*$\cdots$I2$^{ii}$ | 0.89 | 3.10 | 3.63 (2) | 121 |
| N1—H1*B*$\cdots$I1 | 0.89 | 2.76 | 3.63 (2) | 166 |
| N1—H1*C*$\cdots$I1$^{iii}$ | 0.89 | 2.74 | 3.62 (2) | 169 |

Symmetry codes: (i) $x, y-1, z$; (ii) $-x+\frac{3}{2}, y-\frac{1}{2}, z$; (iii) $-x+\frac{5}{2}, y-\frac{1}{2}, z$; (iv) $x+\frac{1}{2}, -y+\frac{3}{2}, z$; (v) $x-\frac{1}{2}, -y+\frac{3}{2}, z$.

octahedral geometry at 223 K, with the bridging Pb1—I2 distances longer than the axial distances Pb1—I1. Phase (I), however, has a terminal distance of 3.2029 (7) Å, longer than the bridging distances to I2 [3.1781 (5) and 3.1836 (5) Å]. The largest deviation from ideal octahedral geometry is seen in the I1—Pb1—I2 *cis* angles, which deviate by 3.85 (7) and 3.576 (19)° for (II) and (I), respectively, from 90°. The *trans* angles are all 180°, by virtue of the inversion centre at the Pb atom. The structure at room temperature has been reported previously and the values for the lead iodide distances and angles agree well with those reported previously (Mitzi, 1996).

The butylammonium cation is on a general position. During the course of the phase transition, the butylammonium cation undergoes possibly the most striking rearrangement, as can be seen in Figs. 10(*c*) and (*d*).

In phase (I), the butylammonium molecule is orientated, in projection, along the long diagonal of the parallelogram formed by adjacent bridging iodide ions. The ammonium group is in close proximity to an acute angle and adopts the right-angled configuration. The hydrogen-acceptor distances to the terminal halide I1 are 2.72 and 2.77 Å, and to the bridging halide I2 2.97 Å (Table 3). Upon cooling, the butylammonium cation moves relative to the parallelogram away from an acute angle to an obtuse angle. The hydrogen-bonding scheme is now equilateral and the hydrogen-acceptor distances to the terminal halide I1 are 2.71 and 3.01 Å, and to the bridging halide I2 2.79 Å. The change from the right-angled to the equilateral geometry goes hand-in-hand with an increase of the tilt angle of the ammonium head group. This angle, $\angle_{\beta}$, almost doubles from 32.2 (2) to 62.7 (6)°.

The movement also affects the general orientation of the butylammonium chain relative to the inorganic layers. In phase (I), the general orientation of the cation is perpendicular to the layers. The C1—C2 and C3—C4 bonds are almost normal to the layers. Upon conversion, the butylamonium cation increases its tilt angle from $\angle_{\varphi}$ = 29.2 (3)° to $\angle_{\varphi}$ = 39.8 (5)° in phase (II). Furthermore, the cation also pivots around its own axis. The plane angle $\angle_{\alpha}$ decreases by 33.5° in going from phase (II) to (I). The movement of the butylammonium ions is accompanied by a decrease in the interlayer spacing by 1.368 Å. The conformation of the butylammonium chain does not change during the phase transition, with the C atoms remaining in an all-*trans* conformation. Hence, this particular phase transition of $C_4$PbI is primarily due to the movement of the essentially rigid butylammonium cations relative to the inorganic layers.

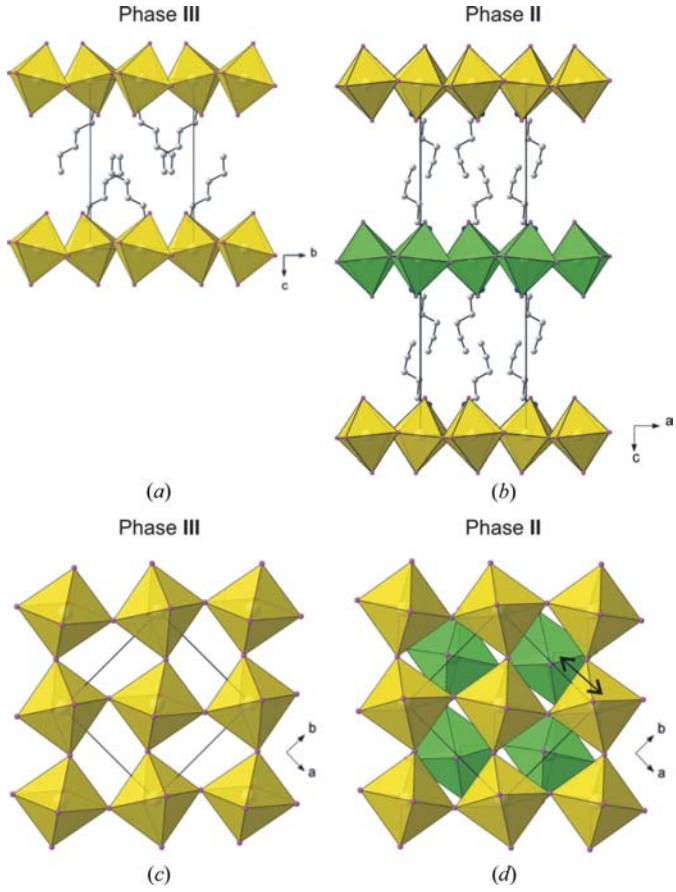


**Figure 11**
The first two phases of $C_5$PbI are shown. Diagram (*a*) shows the packing of phase (III) at 293 K. Diagram (*b*) illustrates the doubling of the unit cell and the change to an orthorhombic system in phase (II). A further difference is the decreasing tilt of the pentylammonium chain in the higher-temperature phase. Diagrams (*c*) and (*d*) are shown perpendicular to the layers; (*c*) shows the eclipsed arrangement of adjacent layers in (III) and (*d*) the staggered layers in (II). In (*b*) and (*d*), the two adjacent layers that are staggered relative to each other are shown in yellow and green. The double-headed arrow indicates the offset of the two adjacent layers in (*d*). H atoms are omitted for clarity in (*a*) and (*b*).

**3.2.2. $C_5PbI$, (III) [(2*b*)] to (II) [(2*c*)].** Figs. 11(*a*) and (*b*) again show a bidimensional arrangement in which two layers of interdigitated pentylammonium cations are embedded between two inorganic [$PbI_6$] sheets, forming the familiar alternating inorganic–organic layered structure. Within the range of temperatures studied, $C_5PbI$ does not undergo any phase transitions below room temperature. The crystal structure of $C_5PbI$ was determined at 173 K, designated (2*a*), and was found to be isostructural to its structure at room temperature, (2*b*), and the geometric parameters show no unexpected variation. In contrast to the phase transition of $C_4PbI$, where the inorganic layers retain their relative positions, the phase behaviour of $C_5PbI$ is more complicated. It involves a movement of the layers as well as a conformational change within the pentylammonium chains. The lead atoms are aligned from layer to layer in phase (III) (2*b*), resulting in an eclipsed arrangement of adjacent layers, typical of layered perovskite-type hybrids with monoclinic unit cells. The space group is $P2_1/a$ and the structure type is based on $RbAlF_4$. The unit cell in (III) contains two inorganic layers at the integral values of $z = 0$ and 1. Consecutive layers are corrugated in the same direction, along the *b* axis. The crystal structure of phase (II), as determined at 363 K (2*c*), has the Pb atoms offset from layer to layer, resulting in a staggered arrangement, typical of layered perovskite-type hybrids with orthorhombic unit cells. The space group of (2*c*) is *Pbca* and its structure type is based on $K_2NiF_4$. The unit cell has doubled in volume to 2356.0 (5) Å$^3$ and now contains three inorganic layers, one layer at $z = 1/2$ and two layers at the same integral values of $z =$ 0 and 1 as in (III). The three inorganic layers are all corrugated along the *a* axis, however, the middle layer is corrugated in the opposite direction to the layers that sandwich it. For adjacent layers to be staggered means that during the phase transition, every second layer in phase (III) has to move half a unit cell in the *a* direction to reach the same staggered packing arrangement as in phase (II) (Fig. 11*d*). The interlayer spacing increases with an increase in temperature from 14.8805 (13) to 14.978 (4) Å.

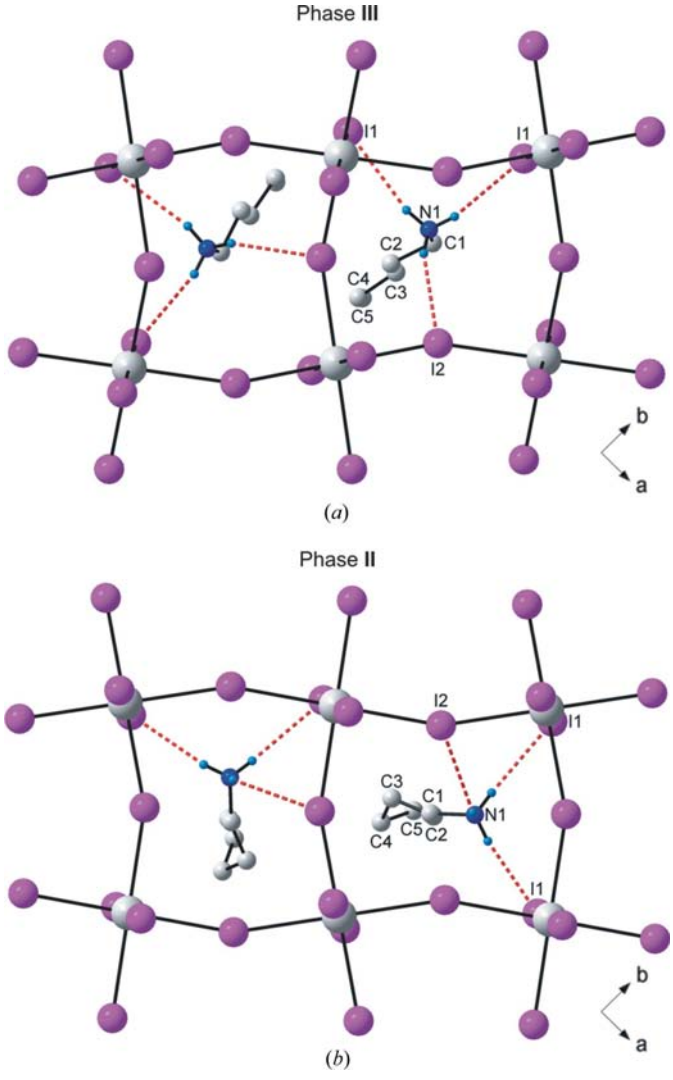


**Figure 12**
Projection of phase (III) of $C_5PbI$ (*a*) and phase (II) (*b*). The pentylammonium chains are flat in (III), whereas C4 is bent out of the plane of the chain in (II). H atoms on C atoms are omitted for clarity.

The same changes in the octahedra in $C_4PbI$ are observed for $C_5PbI$. The asymmetric unit again consists of a Pb atom on a special position and two iodide atoms: I1 occupying the terminal position and I2 occupying the bridging position in the octahedra. The layers are parallel to the *ab* plane in (III) and (II). The $\theta$ tilt of the octahedra relative to each other decreases from 26.32 (3) to 20.99 (11)°. Furthermore, the inorganic layers are corrugated in the *b* direction by an angle of 12.59 (2)° with respect to the *ab* plane in (III) and in the *a* direction by 7.30 (7)° in (II). The bond lengths and angles in the individual $PbI_6$ octahedra behave similarly to those in $C_4PbI$. Phase (III) has axial compression just as phase (II) in $C_4PbI$. The Pb—I1 bond distance in phase (III) is 3.1720 (8) Å and the average Pb—I2 bond distance is 3.1958 (7) Å. After the phase transition, phase II has bridging compression and the difference between the terminal and bridging distances (0.0115 Å) is less than in phase (III) (0.0238 Å). The *trans* angles are 180° and the *cis* angles deviate from 90° by 3.399 (8) and 2.76 (9)°, respectively, for phases (II) and (III).

As in $C_4PbI$, the pentylammonium cations are ordered within the layers in both the $C_5PbI$ phases. At room temperature [phase (III)], the pentylammonium chain is planar and the torsion angles range from 171 (2) to 173.6 (19)°. In phase (II), the C atoms are no longer all in a plane. The N1, C1, C2, C3 and C5 atoms are approximately in a plane, but the C4 atom is bent out of it. The torsion angles C1—C2—C3—C4 and C2—C3—C4—C5 are now −148 (7) and −72 (8)°, respectively.

The pentylammonium chain in phase (III) faces towards the obtuse angled corner of the parallelogram and its hydrogen bonding has the equilateral configuration (see Fig. 12*a*). The hydrogen-acceptor distances to the terminal halide I1 are 2.85 and 2.92 Å, and to the bridging halide I2 2.89 Å. When the compound is heated, the pentylammonium chain aligns itself towards the acute angled position. The hydrogen bonding then displays the right-angled configuration (see Fig. 12*b*). The average hydrogen-acceptor distances to the terminal iodides

**Table 4**
Geometric parameters for all compounds in their phases.

| Geometric parameter | (1*a*), (II) | (1*b*), (I) | (2*a*), (III) | (2*b*), (III) | (2*c*), (II) | (3*a*), (IV) | (3*b*), (III) |
|---|---|---|---|---|---|---|---|
| Interlayer spacing (Å) | 13.117 (5) | 13.8007 (5) | 14.784 (3) | 14.881 (1) | 14.978 (4) | 16.052 (7) | 16.351 (1) |
| Bridging angle Pb1—I2—Pb1 (°) | 149.24 (10) | 155.07 (2) | 150.22 (2) | 153.68 (3) | 159.01 (11) | 155.13 (3) | 155.65 (5) |
| $\theta$ tilt (°) | 30.76 (10) | 24.93 (2) | 29.78 (2) | 26.32 (3) | 20.99 (11) | 24.87 (3) | 24.35 (5) |
| Corrugation $\Psi$ tilt (°) | 12.92 (4) | 5.78 (2) | 12.83 (1) | 12.59 (2) | 7.30 (7) | 5.68 (2) | 5.85 (3) |
| Tilt of chains $\angle_\varphi$ (°) | 39.8 (5) | 29.2 (3) | 30.8 (1) | 29.0 (2) | 19.2 (1) | 32.6 (2) | 21.1 (3) |
| Tilt of plane $\angle_\alpha$ (°) | 55.9 (1) | 88.4 (7) | 67.5 (3) | 70.2 (8) | 87.4 (1) | 75.1 (5) | 89.7 (7) |
| Tilt of $NH_3$ group $\angle_\beta$ (°) | 33.2 (2) | 62.7 (6) | 27.6 (5) | 26.5 (1) | 65.7 (1) | 66.0 (8) | 66.9 (1) |
| Position of ammonium group | Obtuse | Acute | Obtuse | Obtuse | Acute | Acute | Acute |
| Hydrogen-bonding configuration | Equilateral | Right-angled | Equilateral | Equilateral | Right-angled | Right-angled | Right-angled |
| Torsion angle (°) | *Trans* | *Trans* | *Trans* | *Trans* | 138 (9)<br>C1—C2—C3—C4<br>89 (8)<br>C2—C3—C4—C5 | *Trans* | *Trans* |

decrease to 2.65 and 2.80 Å as the $D$—H$\cdots A$ bridging angles increase (Table 3). The angle $\angle_\beta$ at the same time increases from 26.5 (1) to 65.7 (1)° (Table 4). The distance to the bridging iodide increases significantly to 3.12 Å. The $\angle_\varphi$ angle of the chains changes from 29.0 (2) to 19.2 (1)° upon heating, and the $\angle_\alpha$ plane angle changes [70.2 (8) to 87.4 (1)°]. In summary, the phase transition of $C_5PbI$ at 318.4 K from phase (III) to (II) involves a conformational change within the pentylammonium cation, as well as a displacement of the inorganic layers and the pentylammonium cation.

The last phase transition at 391.1 K from phase (II) to (I) was beyond the design specifications of the heating device on the diffractomer so no diffraction data is reported.

**3.2.3. $C_6PbI$, (IV) [(3*a*)] to (III) [(3*b*)]**. The phase behaviour of $C_6PbI$ resembles that of $C_5PbI$. The crystal structure of the monoclinic phase (IV) of $C_6PbI$ (3*a*) was determined at 172 K and crystallizes in the $P2_1/a$ space group with a monoclinic angle of 91.985 (8)°. The asymmetric unit consists of a $Pb_{0.5}I_2$ unit (Pb atom sits on a special position) and a single $C_6H_{13}NH_3^+$ chain. The inorganic layers are then created by sharing the four corner iodides with adjacent octahedra. The Pb atom is on a centre of inversion and has three unique bond distances to the iodides. I1 is terminal and has the longest bond distance of 3.2069 (17) Å. The bridging halide I2 has shorter distances of 3.1608 (13) and 3.1712 (13) Å. The *trans* angles in the octahedra are all 180° with *cis* angles in the range 90.22 (3)–94.61 (3)°. The angle between two Pb atoms bridged by I2 is 155.11 (3)°.

The orthorhombic phase (III) of $C_6PbI$ (3*b*) was structurally characterized at 293 K and crystallizes in the *Pbca* space group. The Pb atom is again situated at a special position. The phase transition at $T_1^c$ = 258 K can be associated with a lateral movement of the layers, perpendicular to the longest axis, relative to each other. This phase (IV) has a monoclinic unit cell and the octahedra lie eclipsed above each other ($RbAlF_4$ structure type). In phase (III), two successive layers are staggered and the octahedra in the adjacent layers are offset (see Fig. 13). The phase change causes the inorganic organic hybrid to convert from the $K_2NiF_4$ to the $RbAlF_4$ structure type. The interlayer spacing increases from 16.052 (7) Å in phase (IV) to 16.372 (1) Å in phase (III).

The hexylammonium chain does not undergo any conformational changes during the phase transition. The plane of the hexylammonium chain changes its orientation relative to the layers, changing from $\angle_\alpha$ = 75.2 (4)° (IV) to $\angle_\alpha$ = 89.6 (8)° (III). Interestingly, there is no change in the position of the ammonium group and the hydrogen bonding has the right-angled configuration in both phases (see Fig. 14). The $\angle_\beta$ angle also remains similar being 66.6 (8)° at 173 K (IV) and 61.3 (1)° at 293 K (III). The change in $\angle_\alpha$ has a slight effect on the hydrogen-bonding geometry. The hydrogen bonds to the terminal iodides are more linear in phase (III), seen in the $D$—H$\cdots A$ angles 169.7 and 171.7°, compared with phase (IV), being 152.5 and 164.2°.

**3.2.4. $C_6PbI$ above room temperature, (III) [(3*b*)] to (II) [(3*c*)] to (I) [(3*d*)]**. We attempted a study of the two phase changes that $C_6PbI$ undergoes above room temperature *via* SC-XRD, on the same crystal used for (3*b*). The phase change at $T_2^h$ = 354.7 K has the highest enthalpy and caused significant

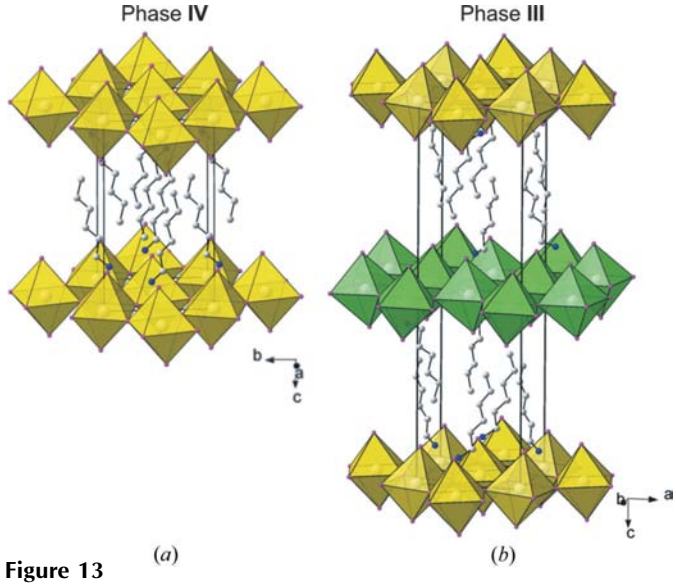


**Figure 13**
Packing diagrams of phase (IV) of $C_6PbI$ (*a*) and phase (III) (*b*). The layers in yellow in both diagrams are eclipsed relative to each other, whereas the green and yellow layers are shown staggered in (*b*). H atoms are omitted for clarity.

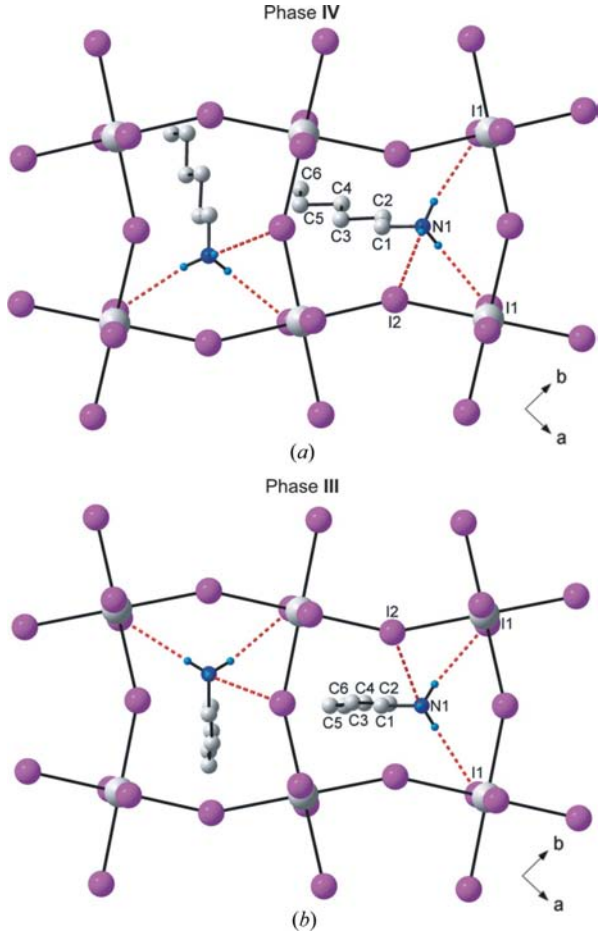


**Figure 14**
The slight orientation change between phase (IV) (*a*) and phase (III) (*b*) of $C_6PbI$. Both phases have the acute position and the right-angled configuration. H atoms on C atoms are omitted for clarity.

damage to the crystal. This is the major transition, where the hexylammonium cation becomes rotationally disordered. The crystal unfortunately fractured significantly, resulting in poor diffraction data that was not suitable for structure solution and refinement. Hence, only the unit-cell parameters are reported (3*c*). The crystal system (orthorhombic) remains the same in this phase as in phase (III). There is an increase in the interlayer spacing from 16.3514 (10) Å [phase (III)] to 17.6212 (36) Å [phase (II)]. The transition from (III) to (II) is presumed to be the chain-melting transition. This conclusion comes from the model of the phase transitions put forward for the compound $[(C_6H_{13}NH_3)_2PbCl_4]$ ($C_6PbCl$), which has four phases (Kammoun & Daoud, 1997). In this compound, the lowest-temperature phase, labelled (IV) by the authors, transforms to phase (III) *via* a first-order, minor phase transition, similar to what is observed in $C_6PbI$. The major transition in $C_6PbCl$ is from phase (II) to phase (I), the final and highest temperature phase. The major transition was attributed to a conformational disorder of the chains, where *gauche* type kinks run through the chains. Furthermore, the orientation of the chains becomes more perpendicular to the inorganic layers, as evidenced by the increase in the interlayer spacing from 17.56 to 19.01 Å, a change of 1.45 Å. The increase in the interlayer spacing in $C_6PbI$ is less as the hexylammonium chains in $C_6PbI$ are interdigitated, whereas in $C_6PbCl$, the chains are non-interdigitated. The same crystal of $C_6PbI$ was then heated further, past the last phase transition at $T_3^h = 371.1$ K, and has a tetragonal unit cell (3*d*). The enthalpy for this phase transition from (II) to (I) is lower (1.1 kJ mol$^{-1}$) than for the previous phase transition from phase (III) to (II) (13.5 kJ mol$^{-1}$) and is presumably due to changes in the inorganic layers only.

## 4. Conclusion

The compounds $[(C_nH_{2n+1}NH_3)_2PbI_4]$ ($n$ = 4, 5 and 6), which belong to the family of inorganic–organic layered perovskite-type hybrids, have one, two and three phase transitions, respectively. Each phase transition is reversible. Only the first phase transition has been investigated by single-crystal structures of the hybrids before and after the first transition. The phase transitions were single-to-single-crystal for $C_4PbI$ (1) and $C_5PbI$ (2), whereas two different crystals were needed for $C_6PbI$ (3). Three major structural changes were observed:

(i) the packing of the inorganic layers changes from staggered to eclipsed in $C_5PbI$ and $C_6PbI$,

(ii) the position of the ammonium group changes relative to the layers from the obtuse to the acute angled position in $C_4PbI$ and $C_5PbI$, and

(iii) the hydrogen-bonding configuration changes from equilateral to right-angled in $C_4PbI$ and $C_5PbI$.

In $C_6PbI$, the cation does not change its position relative to the inorganic layers as drastically as the cations in $C_4PbI$ and $C_5PbI$, which could explain why its phase transition enthalpy is the lowest of the three hybrids for that particular phase transition.

The University of the Witwatersrand and the National Research Fund (GUN 2069064) are thanked for the award of a research grant and for providing the infrastructure required to do this work.

## References

Barman, S., Venkatamaran, N. V., Vasudevan, S. & Seshadri, R. (2003). *J. Phys. Chem. B*, **107**, 1875–1883.
Brandenburg, K. (1999). *DIAMOND*, Version 2.1e. Crystal Impact GbR, Bonn, Germany.
Bruker (2004). *SAINT-PLUS*, Version 7.12 (including *XPREP*). Bruker AXS Inc., Madison, Wisconsin, USA.
Bruker (2005). *APEX*2. Version 1.27. Bruker AXS Inc., Madison, Wisconsin, USA.
Chanh, N. B., Houstry, J. R., Meresse, A., Ricard, L. & Rey-Lafon, M. (1989). *J. Phys. Chem. Solids*, **50**, 829–838.
Chapuis, G. (1978). *Acta Cryst.* B**34**, 1506–1512.
Depmeier, W., Felsche, J. & Wildermuth, G. (1977). *J. Solid State Chem.* **21**, 57–65.
Doudin, B. & Chapuis, G. (1988). *Acta Cryst.* B**44**, 495–502.
Doudin, B. & Chapuis, G. (1990). *Acta Cryst.* B**46**, 175–180.
Dunitz, J. D. (1995). *Acta Cryst.* B**51**, 619–631.
Farrugia, L. J. (1997). *J. Appl. Cryst.* **30**, 565.
Farrugia, L. J. (1999). *J. Appl. Cryst.* **32**, 837–838.

Fernandes, M. A., Levendis, D. C. & Schoening, F. R. L. (2004). *Acta Cryst.* B**60**, 300–314.
Hatch, D. M. & Stokes, H. T. (1987). *Phys. Rev. B: Condens. Matter*, **35**, 8509–8516.
Hatch, D. M., Stokes, H. T., Aleksandrov, K. S. & Misyul, S. V. (1989). *Phys. Rev. B Condens. Matter*, **39**, 9282–9288.
Ishihara, T., Takahashi, J. & Goto, T. (1990). *Phys. Rev. B Condens. Matter*, **42**, 11099–11107.
Kammoun, S. & Daoud, A. (1997). *Phys. Status Solidi. (A)*, **162**, 575–586.
Kato, Y., Ichii, D., Ohashi, K., Kunugita, H., Ema, K., Tanaka, K., Takahashi, T. & Kondo, T. (2003). *Solid State Commun.* **128**, 15–18.
Kataoka, T., Kondo, T., Ito, R., Sasaki, S., Uchida, K. & Miura, N. (1993*a*). *Phys. Rev. B Condens. Matter*, **47**, 2010–2018.
Kataoka, T., Kondo, T., Ito, R., Sasaki, S., Uchida, K. & Miura, N. (1993*b*). *Physica B*, **184**, 132–136.
Kondo, T., Azuma, T., Yuasa, T. & Ito, R. (1998). *Solid State Commun.* **105**, 253–255.
Kondo, T., Iwamoto, S., Hayase, S., Tanaka, K., Ishi, J., Mizuno, M., Ema, K. & Ito, R. (1998). *Solid State Commun.* **105**, 503–506.
Matsuishi, K., Ishihara, T., Onari, S., Chang, Y. H. & Park, C. H. (2004). *Phys. Status Solidi. B*, **241**, 3328–3333.
Mitzi, D. B. (1996). *Chem. Mater.* **8**, 791–800.
Mitzi, D. B. (1999). *Prog. Inorg. Chem.* **48**, 1–121.
Mitzi, D. B. (2001). *J. Chem. Soc. Dalton Trans.* pp. 1–12.
Needham, G. F., Willett, R. D. & Franzen, H. F. (1984). *J. Phys. Chem.* **88**, 674–680.
Sheldrick, G. M. (1997*a*). *SHELXS*97. University of Göttingen, Germany.
Sheldrick, G. M. (1997*b*). *SHELXL*97. University of Göttingen, Germany.
Shibuya, K., Koshimizu, M., Takeoka, T. & Asai, K. (2002). *Nucl. Instrum. Methods Phys. Res. B*, **194**, 207–212.
Spek, A. L. (2003). *J. Appl. Cryst.* **36**, 7–13.
Tanaka, K., Sano, F., Takahashi, T., Kondo, T., Ito, R. & Ema, K. (2002). *Solid State Commun.* **122**, 249–252.
Tanaka, K., Takahashi, T., Kondo, T., Umebayashi, T., Asai, K. & Ema, K. (2005). *Phys. Rev. B Condens. Matter*, **71**, 045312-1-6.